

Subpicosecond metamagnetic phase transition driven by non-equilibrium electron dynamics

Federico Pressacco (✉ federico.pressacco@desy.de)

Deutsches Elektronen-Synchrotron DESY <https://orcid.org/0000-0002-8299-4269>

Davide Sangalli

Istituto di Struttura della Materia—Consiglio Nazionale delle Ricerche (CNR-ISM), Division of Ultrafast Processes in Materials (FLASHit)

Vojtěch Uhlíř

Brno University of Technology <https://orcid.org/0000-0002-0512-6329>

Dmytro Kutnyakhov

DESY Photon Science <https://orcid.org/0000-0002-6294-4600>

Jon Ander Arregi

Brno University of Technology <https://orcid.org/0000-0002-7376-2757>

Steinn Ymir Agustsson

University of Mainz <https://orcid.org/0000-0002-6700-8600>

Günter Brenner

Deutsches Elektronen-Synchrotron DESY, Notkestr. 85, D-22607 Hamburg, Germany

Harald Redlin

Deutsche Elektronen-Synchrotron DESY

Michael Heber

Deutsches Elektronen-Synchrotron DESY

Dmitry Vasilyev

Johannes Gutenberg-Universität Mainz

Jure Demsar

Johannes Gutenberg University Mainz <https://orcid.org/0000-0003-4551-7444>

Gerd Schönhense

Universität Mainz <https://orcid.org/0000-0002-8921-2901>

Matteo Gatti

Plytechnique

Andrea Marini

Consiglio Nazionale delle Ricerche, <https://orcid.org/0000-0001-9289-5750>

Wilfried Wurth

Universität Hamburg

Fausto Sirotti

CNRS <https://orcid.org/0000-0001-8753-8425>

Article

Keywords: Femtosecond Light-induced Phase Transitions, Functional Property Tuning, Time-resolved Photoelectron Spectroscopy, Ferromagnetic Order

Posted Date: February 2nd, 2021

DOI: <https://doi.org/10.21203/rs.3.rs-131654/v1>

License:  This work is licensed under a Creative Commons Attribution 4.0 International License.

[Read Full License](#)

Version of Record: A version of this preprint was published at Nature Communications on August 24th, 2021. See the published version at <https://doi.org/10.1038/s41467-021-25347-3>.

1 Subpicosecond metamagnetic phase transition 2 driven by non-equilibrium electron dynamics

3 Federico Pressacco^{1,2,*}, Davide Sangalli^{3,4}, Vojtěch Uhlíř^{5,6}, Dmytro Kutnyakhov², Jon Ander Arregi⁵,
4 Steinn Ymir Agustsson⁷, Günter Brenner², Harald Redlin², Michael Heber², Dmitry Vasilyev⁷, Jure Demsar⁷,
5 Gerd Schönhense⁷, Matteo Gatti^{8,4,9}, Andrea Marini^{3,4}, Wilfried Wurth^{1,2}, and Fausto Sirotti^{9,10}

6 ¹The Hamburg Centre for Ultrafast Imaging, Hamburg University, Luruper Chaussee 149, 22761, Hamburg, Germany

7 ²DESY Photon Science, Hamburg Germany

8 ³Istituto di Struttura della Materia—Consiglio Nazionale delle Ricerche (CNR-ISM), Division of Ultrafast Processes in Materials
9 (FLASHit), Via Salaria Km 29.5, CP 10, I-00016 Monterotondo Stazione, Italy

10 ⁴European Theoretical Spectroscopy Facility (ETSF)

11 ⁵CEITEC BUT, Brno University of Technology, Purkyňova 123, 612 00 Brno, Czech Republic

12 ⁶Institute of Physical Engineering, Brno University of Technology, Technická 2, 616 69 Brno, Czech Republic

13 ⁷Johannes Gutenberg-Universität, Institute of Physics, Staudingerweg 7, 55128 Mainz, Germany

14 ⁸Laboratoire des Solides Irradiés, École Polytechnique, CNRS, CEA/DRF/IRAMIS, Institut Polytechnique de Paris, F-91128
15 Palaiseau, France

16 ⁹Synchrotron SOLEIL, L'Orme des Merisiers, Saint-Aubin, BP 48, F-91192 Gif-sur-Yvette, France

17 ¹⁰Physique de la Matière Condensée, CNRS and École Polytechnique, IP Paris, F-91128 Palaiseau, France

18 *e-mail: federico.pressacco@desy.de

19 ABSTRACT

Femtosecond light-induced phase transitions between different macroscopic orders provide the possibility to tune the functional properties of condensed matter on ultrafast timescales. In first-order phase transitions, transient non-equilibrium phases and inherent phase coexistence often preclude non-ambiguous detection of transition precursors and their temporal onset. Here, we present a study combining time-resolved photoelectron spectroscopy and ab-initio electron dynamics calculations elucidating the transient subpicosecond processes governing the photoinduced generation of ferromagnetic order in antiferromagnetic FeRh. The transient photoemission spectra are accounted for by assuming that not only the occupation of electronic states is modified during the photoexcitation process. Instead, the photo-generated non-thermal distribution of electrons modifies the electronic band structure. The ferromagnetic phase of FeRh, characterized by a minority band near the Fermi energy, is established 350 ± 30 fs after the laser excitation. Ab-initio calculations indicate that the phase transition is initiated by a photoinduced Rh-to-Fe charge transfer.

21 Introduction

22 Emergence of long-range ordered states in condensed matter is typically a consequence of a fine interplay between the
23 coupled spin, charge, orbital, and lattice degrees of freedom¹⁻⁴. The mechanisms vary between different correlated
24 oxides and metallic systems leading to specific dynamical behavior. Excitation with ultrashort electromagnetic pulses
25 offers the most efficient means to control the physical properties of condensed matter systems on a femtosecond time
26 scale⁵⁻⁷. Materials featuring first-order phase transitions (FOPTs) with abrupt changes in their order parameters are
27 especially appealing for ultrafast devices based on a functionality switch. In this regard, prominent examples are the
28 insulator-metal transition in VO₂^{8,9} or 1T-TaS₂^{10,11}.

29 In order to obtain a good understanding of the relevant mechanisms triggering the transition, it is necessary to
30 explore the fundamental timescale of FOPTs. However, this is often challenging with multiple coupled degrees of
31 freedom displaying complex dynamics upon laser-induced excitation. Moreover, macroscopic phase coexistence at
32 the FOPT, specifically, the processes of nucleation and domain growth, complicate the disentanglement of dynamic
33 changes in order parameters. The fundamental question, whether the modification of electronic structure drives
34 the transition, is extensively debated in the literature, giving key arguments on the role of photoexcited states in
35 double-exchange interactions¹², electronic precursors closing the insulating gap¹³, or the existence of intermediate
36 transient phases^{2,9,14,15}.

37 In the case of ferromagnetic materials, magnetization dynamics triggered by a laser pulse leads to ultrafast
 38 demagnetization¹⁶, associated with changes in the spin polarization^{17–20}, which is impacted by the spin-dependent
 39 mobility of electrons^{21–23}. In contrast, disentangling the ultrafast response of coupled order parameters of magnetic
 40 FOPTs has been far less investigated. Ultrafast generation of ferromagnetic (FM) order has been observed so far
 41 in a relatively small group of materials such as manganites^{1,24} or CuB_2O_4 ²⁵. Understanding the subpicosecond
 42 generation of FM order across a FOPT is still a major challenge in femtomagnetism²⁶.

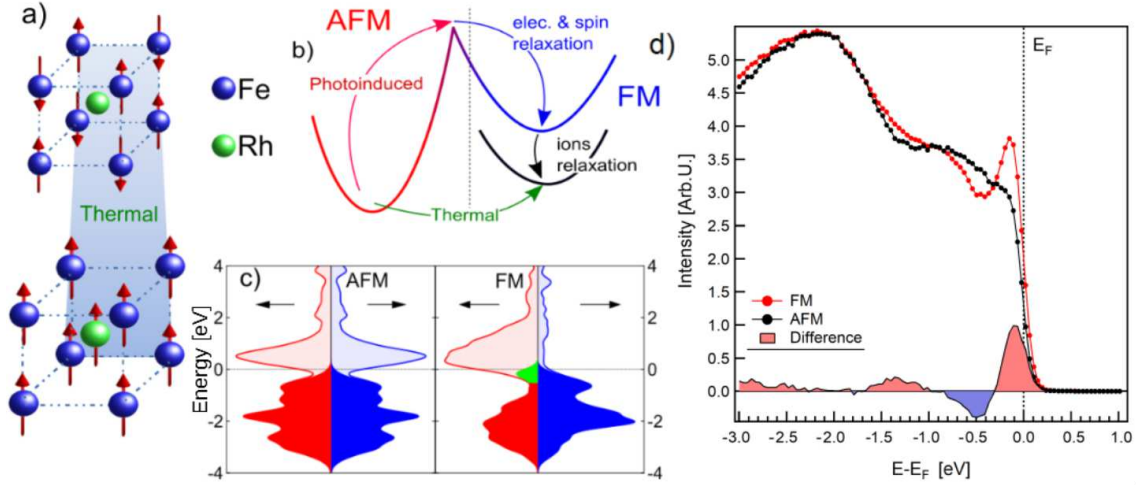


Figure 1. Electronic properties of FeRh across the metamagnetic phase transition. (a) Sketch of the isostructural metamagnetic phase transition in FeRh. At room temperature (top) the system is AFM showing atomic magnetic moments only at the Fe atom sites ($m_{\text{Fe}} = \pm 3.3 \mu_{\text{B}}$). Above 360 K (bottom) the system has ferromagnetically coupled magnetic moments at the Fe ($m_{\text{Fe}} = 3.1 \mu_{\text{B}}$) and Rh ($m_{\text{Rh}} = 0.9 \mu_{\text{B}}$) sites. The whole unit cell expands isotropically by about 1% in volume²⁷. (b) Schematic representation of the two possible paths in the AFM to FM phase transition: direct thermally-driven transition to the FM phase (green arrow), and two-step transition going through a transient electronic state reached during photoexcitation (red arrow) followed by relaxation to the equilibrium FM state (blue and black arrows). (c) Calculated spin-resolved electronic density of states in the AFM and FM phases. The filled areas represent the electronic occupation at thermal equilibrium, with the green area highlighting the position of the Fe minority band (see manuscript text). (d) Measured x-ray photoelectron spectra of FeRh in the AFM (black dots) and FM (red dots) phase. The solid curve at the bottom of the graph is the difference between the two spectra, which allows to appreciate the relative electron density change across the transition. The data correspond to quasi-static thermal cycling experiments prior to the time-resolved measurements.

43 In this work we focus on FeRh, a metallic material that undergoes a metamagnetic FOPT from antiferromagnetic
 44 (AFM) to FM order at $T_M \sim 360$ K and exhibits coupled structural, magnetic and electronic order parameters^{28,29}
 45 (see Fig. 1a). The thermally induced, quasi-static phase transition in FeRh (depicted in Fig. 1b by the green
 46 arrow) has been extensively studied by following the sample magnetization, lattice parameter or resistivity^{30–33}.
 47 Moreover, numerous works have studied the AFM-FM phase transition by means of time-resolved techniques,
 48 where photoexcitation above a threshold intensity results in a nonzero net magnetization. Seminal pump-probe
 49 magneto-optical studies of FeRh films suggested subpicosecond generation of FM order^{34,35}. These results were
 50 discarded by subsequent works, which implied a much slower transition on the order of several picoseconds^{36–39}.
 51 Time-resolved x-ray diffraction indicated that the speed of the transition might be set by the time scale of the
 52 structural changes and thus limited by the speed of sound (~ 5 nm/ps), such that magnetic and structural order
 53 emerge concurrently³⁸. The establishment of long range magnetic order is naturally slower, since it is mediated by
 54 phase boundary expansion, domain coalescence, and magnetic moment alignment. Thus, detection of FM phase via
 55 techniques susceptible to the magnetization direction results in a perceived delay in the emergence of FM order^{36–38}.

56 However, FM order can also be traced by directly exploiting the specifics of the electronic structure, naturally
57 manifested in terms of spin unbalance and the appearance of majority and minority spin bands^{40–42}. This is indepen-
58 dent of spin alignment along a particular direction, and thus allows inspecting FM order via x-ray photoelectron
59 spectroscopy (XPS)^{43–45}. Similar to the electronic signature of the insulator-metal transition^{8,10}, it was demonstrated
60 that the modification of electronic bands might prove equally useful to investigate laser-induced generation of FM
61 order across the magnetic FOPT in FeRh⁴⁶.

62 Here, utilizing time-resolved photoelectron momentum microscopy and supported by first principle calculations,
63 we demonstrate that it is the light-induced modification of the electronic band structure that triggers the phase
64 transition in FeRh. In particular, we show that ultrafast laser excitation induces a charge transfer between the Rh and
65 Fe atoms, serving as a non-equilibrium precursor for the formation of the FM band structure on the subpicosecond
66 timescale.

67 Results

68 The establishment of the FM phase in FeRh is accompanied by the appearance of a narrow peak located about
69 150 meV below the Fermi energy E_F due to the occupation of a spin-polarized Fe band (see green highlighted area
70 in Fig. 1c). The photoelectron spectroscopy data shown in Fig. 1d are the momentum integrated energy distribution
71 curves measured at room temperature for the AFM phase (black dots) and at 420 K for the FM phase (red dots). We
72 use this spectral feature to follow the emergence of the FM phase after laser excitation. Pump-probe experiments
73 were performed at the FLASH Free Electron Laser (FEL) in Hamburg using near-infrared (800 nm, 1.55 eV) pulses
74 of 90 fs coupled with 130 fs soft x-ray pulses with a photon energy of $\hbar\omega = 123.5$ eV (see Methods for details).
75 The laser fluence was 5.6 mJ/cm², which is above the threshold value to induce the FOPT³⁴.

76 Fig. 2a presents the time-resolved, k -integrated photoelectron spectra measured as a function of the delay
77 between the optical pump and x-ray probe pulses, focusing on a 4 ps window around time zero t_0 . One can clearly
78 identify distinct regions in the time-dependent spectra: the temporal overlap between the optical and x-ray pulses
79 (about 100 fs around t_0), the relaxation of electrons towards the Fermi energy on the 100 fs timescale, and the
80 subsequent changes in the density of states near the Fermi level, associated with the formation of the Fe minority
81 band. Differential energy-dependent profiles, reported in Fig. 2b, provide a clearer picture. These are retrieved by
82 averaging the measured photoelectron spectra within a ± 50 fs temporal region for each of the indicated time delays,
83 and subtracting the average photoelectron spectra at negative time delays.

84 The photoexcited electrons relax via electron-electron and electron-phonon scattering, leading to the onset of
85 a Fermi-like distribution (see the red shaded areas for $E - E_F > 0$ in Fig. 2b). A reduction of the electron density
86 below the Fermi level is also observed around t_0 (blue shaded areas for $E - E_F < 0$ in Fig. 2b). At the same delay,
87 the spectrum shows excitation of electrons up to 3.1 eV above E_F (see also the inset in Fig. 3). Note that the electron
88 density above 1.5 eV is almost two orders of magnitude lower. The changes in the population above the Fermi level
89 can be explained by one- and two-photon absorption processes, such that laser excitation ($\hbar\omega_p = 1.55$ eV) promotes
90 electrons into states within the energy range $[E_F, E_F + 2\hbar\omega_p]$. Then, electrons start to relax towards the Fermi level
91 and accumulate in an energy region of a few hundred meV above E_F . On the other hand, the transient depletion of
92 electronic density below the Fermi level is concentrated between -3.1 eV and -1.55 eV $[E_F - 2\hbar\omega_p, E_F - \hbar\omega_p]$.
93 Assuming the photo-induced depletion, one would expect to observe measurable changes in the photoelectron yield
94 only for energies 1.55 eV below the E_F (two photon contribution should be negligible). This suggests that the laser
95 induced changes in the electronic distribution close to the Fermi level cause severe modifications of the deeper lying
96 bands. This implies that the *in-fieri* FOPT involves changes in the overall electronic structure of the system.

97 To elucidate the electronic dynamics near the zero time delay, we compare the experimental results with time-
98 dependent density functional theory (TD-DFT) calculations of the electronic structure performed on FeRh (see
99 Fig. 3). Here, we select a laser fluence which gives a good quantitative agreement with the measured photoelectron
100 spectra. The calculated one- and two-photon absorption intensity above the Fermi level presented in the inset of
101 Fig. 3 corresponds to an excitation of 0.25 electrons per FM unit cell of FeRh (see Fig. 1a), i.e. $\sim 10^{22}$ cm⁻³. This
102 is close to the experimental estimate of 0.15 electrons per unit cell for a 5.6 mJ/cm² fluence. In Fig. 3, the calculated
103 XPS spectrum and its time evolution are obtained considering (i) the time evolution of the electronic distribution

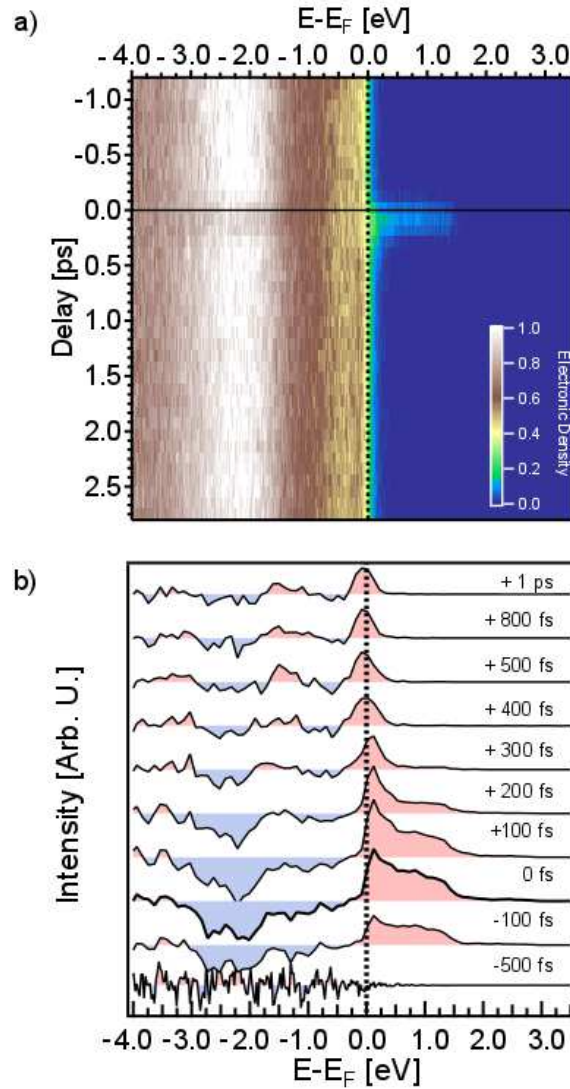


Figure 2. Time-resolved x-ray photoelectron spectroscopy at room temperature. (a) Energy- and delay-dependent matrix of the measured spectra. The vertical dashed line marks the position of the Fermi level E_F , while the horizontal solid line designates the time zero, t_0 . The appearance of electronic density in the unoccupied states is a fingerprint of the laser excitation. We used this spectral feature to identify the temporal overlap between the optical pump and the x-ray probe pulses. (b) Differential photoelectron spectra at selected delays. To enhance the signal to noise ratio, we average the unpumped spectra (between -1 ps and -0.5 ps) and subtract the average spectrum from each row of the matrix. This allows evaluating the statistical noise at negative time delays (-500 fs) as well as accentuating the temporal evolution of the photoelectron spectra. Red and blue shaded areas indicate an increase and a reduction of the electron density with respect to the spectra at negative delays, respectively.

104 function $f_{n\mathbf{k}}(t)$, and (ii) the time evolution of the electronic band structure $\varepsilon_{n\mathbf{k}}(t)$ (see Methods). The changes in
 105 $f_{n\mathbf{k}}(t)$ give rise to a significant signal only in the red and green shaded regions between -1.55 eV and $+1.55$ eV,
 106 while the effect of changes in $\varepsilon_{n\mathbf{k}}(t)$ is most prominent well below the Fermi level. Thus, the signal below -1.55
 107 eV is fully due to changes in $\varepsilon_{n\mathbf{k}}(t)$. The fact that it is negative implies a reduction in the density of states (see the
 108 relative height difference of the red and blue solid curves in Fig. 3).

109 On the other hand, the changes in the region between -1.55 eV and 0 eV result from two effects which sum
 110 to a negligible signal: $f_{n\mathbf{k}}(t)$ gives a negative contribution due to the promotion of electrons into the originally

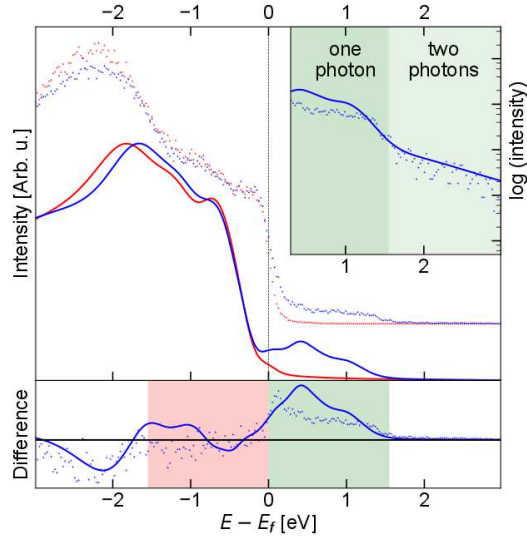


Figure 3. Comparison of experimental and computed photoelectron spectra of FeRh. Spectra at equilibrium ($t = -0.5$ ps) and at the maximum of the pump pulse ($t = 0$ ps) are shown in linear (top panel) and logarithmic scales (inset). The bottom panel exhibits the difference between the two spectra in the top panel. The green (red) region represents the energy range to (from) which electrons are excited with one-photon (1.55 eV) processes. The light green region in the top panel inset identifies the energy range that can be reached by two-photon (3.1 eV) processes.

111 unoccupied states while the change in $\varepsilon_{n\mathbf{k}}(t)$ must result in an increase of the DOS. The region above the Fermi level
 112 seems to be mainly governed by $f_{n\mathbf{k}}(t)$. The overall agreement between theory and experiment is very good. The
 113 observed slight differences may be due to relaxation processes in the experiment already active during the pumping
 114 phase, making the electron distribution more peaked towards the Fermi level.

115 The relaxation of excited electrons proceeds with the formation of a peak above the Fermi level between 100
 116 fs and 300 fs (see Fig. 2b). At a time delay of around 400 fs, the peak crosses the Fermi level and after 500 fs, its
 117 position stabilizes at the energy value which is characteristic for the Fe minority band of the FM phase in FeRh⁴⁶.

118 Further insights into the FOPT dynamics are obtained from the complete differential matrix, presented in Fig. 4a,
 119 monitoring the modification of the electronic density. We selected three energy ranges marked by the red, blue, and
 120 black bars placed on the right hand side of Fig. 4a. The first (red) accounts for the electronic density above 200 meV
 121 and identifies the total number of electrons injected into the unoccupied states upon photoexcitation. The second
 122 (blue) goes from -240 meV to 0 meV and is used to monitor the formation of the Fe minority peak across the phase
 123 transition. The third (black) includes the region from -1.8 eV to -2.8 eV and is used to follow the modification of
 124 deeper bands.

125 Fig. 4b shows the time evolution of the integrated signal in each range. The injection of electrons into the
 126 unoccupied states takes place near zero delay (we recall that our system's response function is 150 fs) and then
 127 rapidly decays (red empty circles), the process being finished by about 500 fs. The intensity at the position of the Fe
 128 minority peak starts to grow already during the laser excitation (filled blue circles), due to both the modification of
 129 the electronic structure and the Fermi level smearing. However, it is only about 300 fs after the excitation that it
 130 displays a fast density increase. The characteristic time delay t_D and subsequent rise time τ of the transition are
 131 obtained by fitting the integrated electron density at the Fe minority peak region with an error function (see Methods)
 132 and yields values of $t_D = 350 \pm 30$ fs and $\tau = 220 \pm 110$ fs. In addition, the data represented by black diamonds in
 133 Fig. 4b, which indicate the time-dependent population of bands in a region below E_F , nearly mirror the population
 134 of the unoccupied levels up to 300 fs, with a fast depletion and recovery. The curve stabilizes thereafter at a finite
 135 value, implying permanent modifications of the deeper bands already after 300 fs, during which the Fe minority

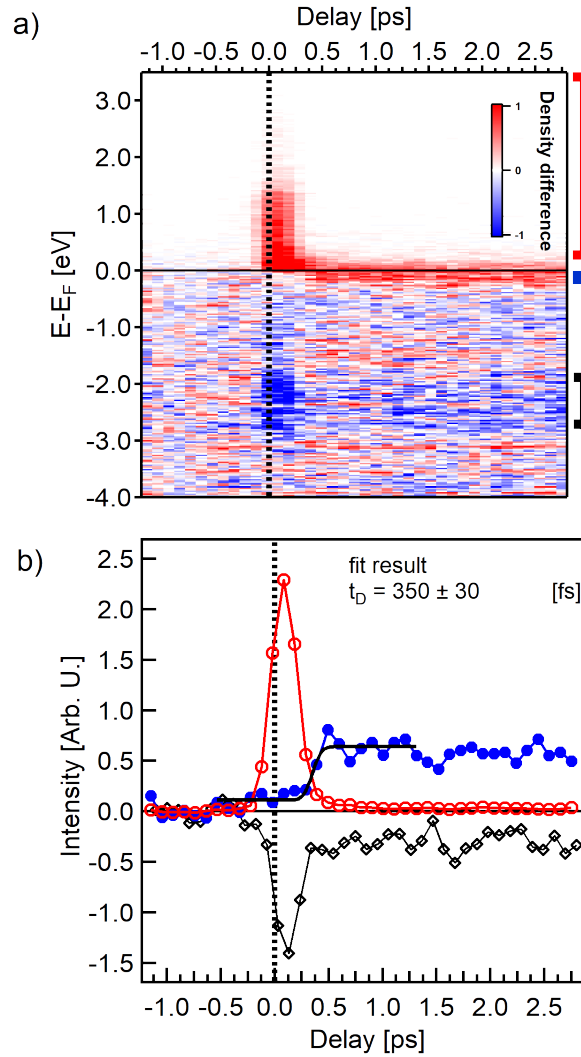


Figure 4. Subpicosecond generation of the electronic FM order in FeRh. (a) Energy- and delay-dependent differential matrix of the measured photoelectron spectra. We subtracted the average of unpumped spectra (between -1 ps and -0.5 ps) from each measured spectrum. The effect of laser excitation is evident around time zero, indicating depletion of the occupied states and the corresponding population of the empty states. In addition, an increase in the electronic density close to the Fermi level is observed at positive time delays. The red, blue, and black bars on the right hand side mark the representative integration regions for tracking the electronic dynamics in the unoccupied states, the formation of the Fe minority peak, and the modification of the deeper bands, respectively. (b) Temporal evolution of the electronic density in the three characteristic energy regions marked in (a). The population of states above the Fermi level shows a fast rise and a consecutive decay around t_0 (empty red circles). The deeper bands (empty black diamonds) show a corresponding depletion and recovery which reflects the dynamics of the unoccupied states. However, their occupation level stabilizes 300 fs after t_0 and remains constant thereafter. The electronic density slightly below E_F (filled blue circles) shows a moderate increase during the laser excitation up to 300 fs delay, followed by a pronounced increase due to the shift of Fe minority band below E_F at a delay t_D of 350 fs. This value was extracted by fitting the error function to the experimental results (black solid line). Subsequently, the minority Fe band peak intensity remains constant throughout the investigated delay range.

136 peak is still shifting towards its final position at 150 meV below E_F . Similar differences in the behaviour of the
 137 electronic density at and below the Fermi level have been observed during ultrafast demagnetization process in Fe¹⁷

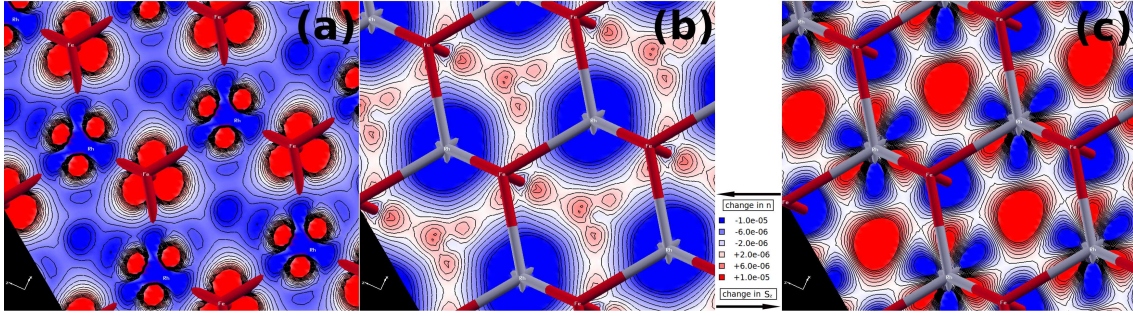


Figure 5. Computed photoinduced changes in charge and spin density in FeRh. (a, b) Changes in the charge density $n(\mathbf{r}, t_f) - n^{eq}(\mathbf{r})$ and (c) spin density $S_z(\mathbf{r}, t_f) - S_z^{eq}(\mathbf{r})$ at the end of the laser pulse ($t = t_f$) with respect to the equilibrium configuration. Densities are represented in atomic units on two different FeRh{111}-planes: the plane just below the $Fe(\uparrow)$ atoms (panel a) and the plane containing the Rh atoms (panels b, c). Fe and Rh atom positions are indicated by red and grey segments of the lattice, respectively. Charge is transferred from the occupied (bonding) orbitals of Rh atoms (panel b), to the unoccupied (anti-bonding) orbitals of Rh and Fe (panel a). Since the Fe anti-bonding levels are filled in this process, the local Fe spin density is reduced. As a result, there is a redistribution of spin density around the Rh atoms and a reduction of the local spin moment at the Fe atoms (panel c). The movies in the **Supplementary Information** show the simulated time evolution of the charge density variations at the Fe and Rh sites as represented in panels (a) and (b) at the beginning and the end of the laser pulse.

138 and Co¹⁸. In the present case, this behavior shows that the FOPT in FeRh is mediated by a transient electronic phase
 139 in which the electronic structure is different from both the AFM and FM phases. The transient phase exists in a
 140 delay range from up to 500 fs after laser excitation.

141 Discussion

142 The unexpected reduction of the photoelectron yield below the one-photon absorption range (~ 1.55 eV), an energy
 143 region where the electronic populations $f_{nk}(t)$ cannot be strongly affected by the laser excitation, is explained
 144 by theoretical calculations. The effect can only be accounted for by considering the photoinduced change in the
 145 electronic band structure (i.e. density of states). Time-resolved XPS spectra are usually described and interpreted in
 146 terms of changes in the population $f_{nk}(t)$ only. This is clearly insufficient for the ultrafast dynamics in FeRh, since
 147 changes in $\varepsilon_{nk}(t)$ must be considered on the same level even before the phase transition is complete.

148 The changes in $\varepsilon_{nk}(t)$ during and after photoexcitation provide insights into why FeRh would relax towards the
 149 FM phase. The photoexcitation process in the AFM state depletes the valence states, which are characterised by
 150 hybridized Fe-Rh bonding states, and fills the unoccupied states, where empty Fe “local minority-spin” anti-bonding
 151 states are mainly available. As a result two processes occur: a charge (and spin) transfer from Rh to Fe ($Rh \rightarrow Fe$),
 152 and a symmetric spin transfer from Fe “local majority” \rightarrow Fe “local minority” ($Fe(\uparrow) \leftrightarrow Fe(\downarrow)$). Simulated charge
 153 and spin density changes upon photoexcitation clearly show this, Fig. 5. Here, the blue regions around the Rh atoms
 154 indicate a charge depletion, which can only partially be explained by a local redistribution. Most of the charge is
 155 transferred to the Fe atoms (see Fig. 5a), while there is a strong charge depletion around Rh atoms (see Fig. 5b).
 156 The $Rh \rightarrow Fe$ process also increases the spin density around the Rh atoms (see Fig. 5c). On the other hand, the
 157 $Fe(\uparrow) \leftrightarrow Fe(\downarrow)$ is a pure spin transfer process, with a strong reduction ($\sim 10\%$) of the local momentum of the Fe
 158 atoms, which is transferred into the vicinity of the Rh atoms (see Fig. 5c).

159 In the AFM phase, the zero magnetic moment around the Rh atoms is a result of a non-vanishing spin density
 160 that integrates to zero because of the hybridization with surrounding Fe atoms with opposite moments^{3,42,47}. The
 161 photoexcitation alters this delicate balance. As shown for the magnetic disorder associated with the temperature
 162 increase, the decrease of the Fe-Fe first-neighbor AFM couplings favors the FM order of the Fe subsystem, while
 163 inducing magnetic fluctuations on the Rh sites³. In turn, the induced Rh magnetic moments stabilize the FM over the
 164 AFM state^{3,34,48,49}. Our simulations therefore suggest that the change of Fe-Rh hybridization ($Rh \rightarrow Fe$ process)

165 plays a critical role in the photoinduced transition. The $Fe(\uparrow) \leftrightarrow Fe(\downarrow)$ process corresponds to the intersite spin
166 transfer which has been recently proposed, on the basis of TD-DFT simulations, as a key mechanism also in other
167 multicomponent magnetic materials^{50–52}. Here, it causes to weaken the AFM ordering but is not sufficient to trigger
168 the magnetic transition alone (just after the photoexcitation, the system is still in the AFM phase).

169 The theoretical simulation, not including dissipating effects, cannot describe the dynamics after the photoexcita-
170 tion when electron-electron, electron-phonon and electron-magnon interactions are at play, and the actual phase
171 transition takes place. Taking into account dissipating effects, one would expect further dynamics of both $f_{nk}(t)$ and
172 $\epsilon_{nk}(t)$: the formation of a Fermi distribution and its subsequent cooling (for $f_{nk}(t)$), and the formation of the FM
173 band structure (for $\epsilon_{nk}(t)$). Instead, our experimental time resolution is fast enough to allow the identification of a
174 bottleneck time in this process, i.e., the metamagnetic transformation exhibiting a 350 fs delay. It is associated with
175 a change in the band structure, with the spin-minority Fe band slightly pushed below the Fermi level and getting
176 filled by the electrons that progressively cool down. This transformation occurs on a subpicosecond timescale that is
177 faster than what was determined by previous experiments on FeRh with a lower time resolution⁴⁶. Most importantly,
178 our results set a new timescale that is faster than the lattice expansion and the establishment of the macroscopic,
179 long-range magnetic order^{36–38}.

180 The process is schematically depicted in Fig. 1b. Immediately after the action of the pulse, a significant number
181 of electrons is excited to unoccupied states, with a non-thermal distribution of electrons $f_{nk}(t)$ (red arrow in Fig. 1b)
182 decaying towards the Fermi level on a time scale of about 200 fs. This is accompanied by the slower dynamics of
183 the band structure ϵ_{nk} with the formation of the peak of the Fe minority band. The peak crosses the Fermi level at
184 about 350 fs delay, and stabilizes at -150 meV binding energy after 400 fs. During this step, the system undergoes
185 a purely electronic transition through a transient phase, where the electronic band configuration evolves from $\epsilon_{nk}(t)$
186 to an intermediate electronic FM phase ϵ_{nk}^{e-FM} (blue arrow in Fig. 1b). Once the electronic distribution reaches the
187 configuration of the FM phase (after 400 fs), the relaxation of the lattice parameter towards the equilibrium value of
188 the FM phase then follows on a longer time scale (black arrow in Fig. 1b).

189 Conclusion

190 In conclusion, we determine the existence of a transient electronic phase needed to induce the AFM to FM
191 phase transition of FeRh using pump-probe photoelectron spectroscopy at the FLASH FEL facility. The results
192 are supported by electronic structure calculations, which explain the details of the dynamics following the laser
193 excitation. The time-resolved photoemission experiment at a laser fluence of 5.6 mJ/cm² is well reproduced assuming
194 the excitation of 0.25 electrons per unit cell of FeRh. At these fluences, the photon absorption cannot be described
195 simply as promotion of electrons from filled to empty states of the calculated band structure, but the modified
196 electron population induces a modification of the band structure as well, which is confirmed by the good agreement
197 between theory and experiments. The laser excitation results in the transfer of electrons from the occupied d orbitals
198 below the Fermi level to the unoccupied d orbitals above the Fermi level, with a partial transfer of electrons from the
199 Rh to the Fe sites. The transient electronic phase exists up to 500 fs after the laser excitation. The emergence of
200 the FM phase can be followed by the appearance and position of the Fe minority band near the Fermi level with
201 characteristic time of $\tau = 220 \pm 110$. Photoexcited electrons relax across the Fermi level and establish the FM
202 electronic band structure 400 fs after the laser excitation. We thus conclude that metamagnetism in FeRh is triggered
203 on a subpicosecond time scale. Further exploration of the laser-induced dynamics in ultrathin and nanoscale confined
204 FeRh³² could lead to ultrafast devices based on magnetic order-order phase transitions at room temperature.

205 Methods

206 **Sample and surface preparation.** The sample consists of an epitaxial 80-nm-thick FeRh(001) film grown onto a
207 MgO(001) substrate by dc magnetron sputtering using an equiatomic target. The films were grown at 725 K and
208 post-annealed in situ at 1070 K for 45 minutes in order to achieve CsCl-type chemical ordering. Upon cooling
209 down the samples in the ultra high vacuum chamber, single-layer graphene is formed on top of the FeRh surface by
210 segregating the carbon from the film⁵³. This provides oxidation protection in air and avoids the need for further
211 capping layers of the FeRh layer to be transported to the FEL facility without degradation. The good quality of the
212 crystallographic texture and the existence of the magnetic phase transition were confirmed using x-ray diffraction
213 and vibrating sample magnetometry, respectively⁵⁴. The sample surface was prepared via annealing only, in order
214 to preserve the graphene layer, and tested with XPS prior to the time-resolved experiments as described in earlier
215 works^{42,46}. Examination with low-energy electron diffraction revealed the expected reconstruction pattern of the
216 FeRh(001) surface.

217 **Experiment.** The experiments are performed at the plane grating monochromator beamline^{55,56} at FLASH^{57,58},
218 using the HEXTOF end-station⁵⁹. The pump-probe scheme is established by a near-infrared pulse of 90 fs coupled
219 with a FEL pulse of about 130 fs (both values are the full width half maximum, FWHM), which provide an estimated
220 system response function⁵⁹, i.e., the effective pump-probe correlation, of ~ 150 fs FWHM. The optical pump
221 and x-ray probe energies were set to 1.55 eV and 123.5 eV, respectively. The energy resolution of ~ 150 meV is
222 extracted from the Fermi level fit.

Photoexcited electrons near normal emission were detected using a momentum microscope, which has an acceptance angle of 2π above the sample surface and can image the full Brillouin zone (BZ) with up to 7 \AA^{-1} diameter^{59,60}. We used a negative extractor voltage (~ 40 V with respect to the sample potential). This retarding field between the sample and extractor effectively removes the slow secondary electrons originating from the x-ray photons and pump-laser-induced slow electrons. All background electrons with energies less than ~ 4 eV are thus repelled within the first 400 μm above the sample surface. This removal of space charge comes at the expenses of k -resolution and causes a reduction of the k -field-of-view to 1.3 \AA^{-1} . Integrating over this k -field represents the integral of 60% of the BZ of FeRh, which was sufficient to well identify the peak associated with the FM phase. We characterize the sample surface by measuring the spectra of the system in the AFM and FM phases at fixed temperatures, and obtained line-shapes equivalent to those reported in ref. 46 (see Fig. 1d). The presence of the peak at about ~ 150 meV below the Fermi level is the signature of the Fe minority band characteristic of the FM phase. To fit the experimental data in Fig. 4b, we used an error function of the following form:

$$f(t) = y_0 + A \left[1 + \text{erf} \left(\frac{t - t_D}{\tau} \right) \right]$$

223 where y_0 is a vertical offset, A is the amplitude, t_D is the temporal onset of the transition (with respect to t_0), and τ is
224 the characteristic rise time.

225 **Theory.** We calculate from first principles the equilibrium and non-equilibrium properties of FeRh using the `pw.x`
226 and `yambo` codes⁶¹⁻⁶⁴ within Density Functional Theory (DFT) and its Time Dependent (TD-DFT) extension.
227 At equilibrium both the FM and AFM phases are computed within the local density approximation (LDA) fully
228 including spin-orbit coupling (SOC). An energy cut-off of 65 Ry is used for the wave-functions with a $5 \times 5 \times 5$
229 sampling of the BZ for the self-consistent calculation. The experimental lattice parameter, 5.966 \AA , is chosen for the
230 AFM structure: an FCC unit cell containing 4 atoms (there is a factor 2 compared to the parameter of the BCC unit
231 cell with 2 atoms used in ref. 65). The FM ground state is then computed for the same unit cell and for a unit cell
232 with a 1% lattice expansion. LDA gives a low negative stress using the experimental value of the lattice parameters
233 in both the FM and the AFM phase. We use the experimental values and we verified that changes in the lattice
234 parameters very weakly affect the electronic density of states.

235 We also verified that the Generalized Gradient Approximation (GGA) gives small improvements in comparison
236 with experimental values, which however are not relevant to the present work. For this reason we used LDA which

237 is more easily handled in the non equilibrium TD–DFT simulations with SOC. Finally we verified that the AFM
238 structure displays a phonon instability as reported in the literature^{65–67}.

239 Subsequently, a non self-consistent calculation (NSCF) on a $8 \times 8 \times 8$ sampling of the BZ is performed. The
240 electronic density of states (DOS) of the two structures reported in Fig. 1c is computed starting from such NSCF
241 calculation. We then construct the XPS spectrum from the projection of the DOS on the atomic orbitals of Fe
242 and Rh. The projected DOS are weighted using tabulated photoionization cross sections⁶⁸ for a probe of 125 eV
243 (in practice the signal is dictated by Fe(3d) orbitals). Moreover, we use energy dependent lifetimes of the form
244 $\gamma_{nk} = A + Bd(\epsilon_{nk}) + C(\epsilon_F - \epsilon_{nk})^2$, where the first constant contribution $A = 60$ meV mimics the experimental
245 resolution, the second term B , proportional to the electronic DOS $d(\epsilon)$, mimics the electron–phonon lifetimes and,
246 finally, the term which grows quadratically away from the Fermi level mimics the electron–electron lifetimes. Finally,
247 the effect of temperature is included in the Fermi distribution used for the electronic occupations. The resulting
248 spectrum is shown in Fig. 1c.

249 The TD–DFT simulations, as implemented in the `yambo` code⁶⁹, are then performed propagating the Kohn–
250 Sham density matrix in the basis–set of the equilibrium wave–functions under the action of the same pump pulse used
251 in the experiment. The NSCF DFT calculation is used as a starting point for TD–DFT. The laser pulse parameters
252 are equivalent to the experimental conditions. In particular, the fluence is chosen considering: (i) the experimental
253 fluence, (ii) the fact that part of the pulse is reflected by the sample, and (iii) the fact that the external field is
254 renormalized by the induced field. The effect of both (ii) and (iii) is estimated taking into account the dielectric
255 function of bulk FeRh. In particular, point (iii) needs to be considered since we adopt the so called transverse gauge,
256 where the macroscopic (or $G = 0$) component of the Hartree field is subtracted from the microscopic TD–DFT
257 equations. The density matrix is calculated on a $8 \times 8 \times 8$ grid of \mathbf{k} points in the BZ including all states from
258 -3.5 up to 5.5 eV. The Kohn–Sham field felt by the electrons is updated at each time step during the simulation.
259 The non-equilibrium DOS is then computed by diagonalizing the Hamiltonian evaluated from the photoexcited
260 electron density after the action of the pump pulse. The adiabatic non-equilibrium XPS spectrum is finally computed
261 using the same smearing used for the equilibrium spectra. The electronic occupation is obtained from the diagonal
262 elements of the density matrix in the basis updated during the course of the simulation.

263 References

- 264 1. Li, T., Patz, A., Mouchliadis, L., Yan, J., Lograsso, T. A., Perakis, I. E. & Wang, J. Femtosecond switching
265 of magnetism via strongly correlated spin–charge quantum excitations. *Nature* **496**, 69–73 (2013). URL
266 <https://doi.org/10.1038/nature11934>.
- 267 2. De Jong, S. *et al.* Speed limit of the insulator–metal transition in magnetite. *Nat. Mater.* **12**, 882–886 (2013).
268 URL <https://doi.org/10.1038/nmat3718>.
- 269 3. Polesya, S., Mankovsky, S., Ködderitzsch, D., Minár, J. & Ebert, H. Finite-temperature magnetism of FeRh
270 compounds. *Phys. Rev. B* **93**, 024423 (2016). URL [https://doi.org/10.1103/PhysRevB.93.](https://doi.org/10.1103/PhysRevB.93.024423)
271 [024423](https://doi.org/10.1103/PhysRevB.93.024423).
- 272 4. Wollmann, L., Nayak, A. K., Parkin, S. S. & Felser, C. Heusler 4.0: Tunable Materials. *Annu. Rev. Mater. Res.*
273 **47**, 247–270 (2017). URL <https://doi.org/10.1146/annurev-matsci-070616-123928>.
- 274 5. Rohwer, T. *et al.* Collapse of long-range charge order tracked by time-resolved photoemission at high momenta.
275 *Nature* **471**, 490–493 (2011). URL <https://doi.org/10.1038/nature09829>.
- 276 6. Fausti, D., Tobey, R., Dean, N., Kaiser, S., Dienst, A., Hoffmann, M. C., Pyon, S., Takayama, T., Takagi, H. &
277 Cavalleri, A. Light-induced superconductivity in a stripe-ordered cuprate. *Science* **331**, 189–191 (2011). URL
278 <https://doi.org/10.1126/science.1197294>.
- 279 7. Singer, A. *et al.* Photoinduced Enhancement of the Charge Density Wave Amplitude. *Phys. Rev. Lett.* **117**,
280 056401 (2016). URL <https://doi.org/10.1103/PhysRevLett.117.056401>.

- 281 **8.** Wegkamp, D. *et al.* Instantaneous Band Gap Collapse in Photoexcited Monoclinic VO₂ due to Photocarrier
282 Doping. *Phys. Rev. Lett.* **113**, 216401 (2014). URL [https://doi.org/10.1103/PhysRevLett.113.](https://doi.org/10.1103/PhysRevLett.113.216401)
283 [216401](https://doi.org/10.1103/PhysRevLett.113.216401).
- 284 **9.** Shao, Z., Cao, X., Luo, H. & Jin, P. Recent progress in the phase-transition mechanism and modulation of
285 vanadium dioxide materials. *NPG Asia Mater.* **10**, 581–605 (2018). URL [https://doi.org/10.1038/](https://doi.org/10.1038/s41427-018-0061-2)
286 [s41427-018-0061-2](https://doi.org/10.1038/s41427-018-0061-2).
- 287 **10.** Perfetti, L., Loukakos, P. A., Lisowski, M., Bovensiepen, U., Berger, H., Biermann, S., Cornaglia, P. S., Georges,
288 A. & Wolf, M. Time Evolution of the Electronic Structure of 1T-TaS₂ through the Insulator-Metal Transition.
289 *Phys. Rev. Lett.* **97**, 067402 (2006). URL <https://doi.org/10.1103/PhysRevLett.97.067402>.
- 290 **11.** Stojchevska, L., Vaskivskiy, I., Mertelj, T., Kusar, P., Svetin, D., Brazovskii, S. & Mihailovic, D. Ultrafast
291 Switching to a Stable Hidden Quantum State in an Electronic Crystal. *Science* **344**, 177–180 (2014). URL
292 <https://doi.org/10.1126/science.1241591>.
- 293 **12.** Ono, A. & Ishihara, S. Double-Exchange Interaction in Optically Induced Nonequilibrium State: A Conversion
294 from Ferromagnetic to Antiferromagnetic Structure. *Phys. Rev. Lett.* **119**, 207202 (2017). URL <https://doi.org/10.1103/PhysRevLett.119.207202>.
- 296 **13.** Gray, A. X. *et al.* Correlation-Driven Insulator-Metal Transition in Near-Ideal Vanadium Dioxide Films. *Phys.*
297 *Rev. Lett.* **116**, 116403 (2016). URL <https://doi.org/10.1103/PhysRevLett.116.116403>.
- 298 **14.** Wall, S., Foglia, L., Wegkamp, D., Appavoo, K., Nag, J., Haglund, R. F., Stähler, J. & Wolf, M. Tracking the evo-
299 lution of electronic and structural properties of VO₂ during the ultrafast photoinduced insulator-metal transition.
300 *Phys. Rev. B* **87**, 115126 (2013). URL <https://doi.org/10.1103/PhysRevB.87.115126>.
- 301 **15.** Morrison, V. R., Chatelain, R. P., Tiwari, K. L., Hendaoui, A., Bruhács, A., Chaker, M. & Siwick, B. J. A
302 photoinduced metal-like phase of monoclinic VO₂ revealed by ultrafast electron diffraction. *Science* **346**,
303 445–448 (2014). URL <https://doi.org/10.1126/science.1253779>.
- 304 **16.** Beaupaire, E., Merle, J.-C., Daunois, A. & Bigot, J.-Y. Ultrafast Spin Dynamics in Ferromagnetic Nickel.
305 *Phys. Rev. Lett.* **76**, 4250–4253 (1996). URL <https://doi.org/10.1103/PhysRevLett.76.4250>.
- 306 **17.** Gort, R. *et al.* Early Stages of Ultrafast Spin Dynamics in a 3d Ferromagnet. *Phys. Rev. Lett.* **121**, 087206
307 (2018). URL <https://doi.org/10.1103/PhysRevLett.121.087206>.
- 308 **18.** Eich, S. *et al.* Band structure evolution during the ultrafast ferromagnetic-paramagnetic phase transition in
309 cobalt. *Sci. Adv.* **3**, e1602094 (2017). URL <https://doi.org/10.1126/sciadv.1602094>.
- 310 **19.** Tengdin, P. *et al.* Critical behavior within 20 fs drives the out-of-equilibrium laser-induced magnetic phase tran-
311 sition in nickel. *Sci. Adv.* **4**, eaap9744 (2018). URL <https://doi.org/10.1126/sciadv.aap9744>.
- 312 **20.** Andres, B. & Weinelt, M. Spin-resolved electronic structure of 3d transition metals during ultrafast demagneti-
313 zation. *J. Magn. Magn. Mater.* **501**, 166475 (2020). URL [https://doi.org/10.1016/j.jmmm.2020.](https://doi.org/10.1016/j.jmmm.2020.166475)
314 [166475](https://doi.org/10.1016/j.jmmm.2020.166475).
- 315 **21.** Eschenlohr, A., Battiato, M., Maldonado, P., Pontius, N., Kachel, T., Holldack, K., Mitzner, R., Föhlisch, A.,
316 Oppeneer, P. M. & Stamm, C. Ultrafast spin transport as key to femtosecond demagnetization. *Nat. Mater.* **12**,
317 332–336 (2013). URL <https://doi.org/10.1038/nmat3546>.
- 318 **22.** Bergeard, N., Hehn, M., Mangin, S., Lengaigne, G., Montaigne, F., Lalieu, M. L. M., Koopmans, B. &
319 Malinowski, G. Hot-Electron-Induced Ultrafast Demagnetization in Co/Pt Multilayers. *Phys. Rev. Lett.* **117**,
320 147203 (2016). URL <https://doi.org/10.1103/PhysRevLett.117.147203>.
- 321 **23.** Carva, K., Battiato, M., Legut, D. & Oppeneer, P. M. Ab initio theory of electron-phonon mediated ultrafast
322 spin relaxation of laser-excited hot electrons in transition-metal ferromagnets. *Phys. Rev. B* **87**, 184425 (2013).
323 URL <https://doi.org/10.1103/PhysRevB.87.184425>.

- 324 **24.** Matsubara, M., Okimoto, Y., Ogasawara, T., Tomioka, Y., Okamoto, H. & Tokura, Y. Ultrafast Photoinduced
325 Insulator-Ferromagnet Transition in the Perovskite Manganite $\text{Gd}_{0.55}\text{Sr}_{0.45}\text{MnO}_3$. *Phys. Rev. Lett.* **99**, 207401
326 (2007). URL <https://doi.org/10.1103/PhysRevLett.99.207401>.
- 327 **25.** Bossini, D., Konishi, K., Toyoda, S., Arima, T., Yumoto, J. & Kuwata-Gonokami, M. Femtosecond ac-
328 tivation of magnetoelectricity. *Nat. Phys.* **14**, 370–374 (2018). URL <https://doi.org/10.1038/s41567-017-0036-1>.
- 330 **26.** Kirilyuk, A., Kimel, A. V. & Rasing, T. Ultrafast optical manipulation of magnetic order. *Rev. Mod. Phys.* **82**,
331 2731–2784 (2010). URL <https://doi.org/10.1103/RevModPhys.82.2731>.
- 332 **27.** Shirane, G., Chen, C., Flinn, P. & Nathans, R. Hyperfine fields and magnetic moments in the Fe–Rh system. *J.*
333 *Appl. Phys.* **34**, 1044–1045 (1963). URL <https://doi.org/10.1063/1.1729362>.
- 334 **28.** Fallot, M. & Hocart, R. Sur l'apparition du ferromagnétisme par élévation du température dans des alliages
335 de fer et de rhodium. *Rev. Sci.* **77**, 498–501 (1939). URL <https://gallica.bnf.fr/ark:/12148/bpt6k6566471c/f508.item>.
- 337 **29.** Kouvel, J. S. & Hartelius, C. C. Anomalous magnetic moments and transformations in the ordered alloy FeRh.
338 *J. Appl. Phys.* **33**, 1343–1344 (1962). URL <https://doi.org/10.1063/1.1728721>.
- 339 **30.** Maat, S., Thiele, J.-U. U. & Fullerton, E. E. Temperature and field hysteresis of the antiferromagnetic-to-
340 ferromagnetic phase transition in epitaxial FeRh films. *Phys. Rev. B* **72**, 214432 (2005). URL <https://doi.org/10.1103/PhysRevB.72.214432>.
- 342 **31.** Baldasseroni, C., Bordel, C., Gray, A. X., Kaiser, A. M., Kronast, F., Herrero-Albillos, J., Schneider, C. M.,
343 Fadley, C. S. & Hellman, F. Temperature-driven nucleation of ferromagnetic domains in FeRh thin films. *Appl.*
344 *Phys. Lett.* **100**, 262401 (2012). URL <https://doi.org/10.1063/1.4730957>.
- 345 **32.** Uhlíř, V., Arregi, J. A. & Fullerton, E. E. Colossal magnetic phase transition asymmetry in mesoscale FeRh
346 stripes. *Nat. Commun.* **7**, 13113 (2016). URL <https://doi.org/10.1038/ncomms13113>.
- 347 **33.** Keavney, D. J., Choi, Y., Holt, M. V., Uhlíř, V., Arena, D., Fullerton, E. E., Ryan, P. J. & Kim, J.-W. Phase
348 coexistence and kinetic arrest in the magnetostructural transition of the ordered alloy FeRh. *Sci. Rep.* **8**, 1778
349 (2018). URL <https://doi.org/10.1038/s41598-018-20101-0>.
- 350 **34.** Ju, G., Hohlfeld, J., Bergman, B., Van Devedonk, R. J. M., Mryasov, O. N., Kim, J. Y., Wu, X., Weller, D. &
351 Koopmans, B. Ultrafast generation of ferromagnetic order via a laser-induced phase transformation in FeRh
352 thin films. *Phys. Rev. Lett.* **93**, 197403 (2004). URL <https://doi.org/10.1103/PhysRevLett.93.197403>.
- 354 **35.** Thiele, J.-U., Buess, M. & Back, C. H. Spin dynamics of the antiferromagnetic-to-ferromagnetic phase
355 transition in FeRh on a sub-picosecond time scale. *Appl. Phys. Lett.* **85**, 2857–2859 (2004). URL <https://doi.org/10.1063/1.1799244>.
- 357 **36.** Bergman, B., Ju, G., Hohlfeld, J., van de Veerdonk, R. J. M., Kim, J.-Y., Wu, X., Weller, D. & Koopmans, B.
358 Identifying growth mechanisms for laser-induced magnetization in FeRh. *Phys. Rev. B* **73**, 060407(R) (2006).
359 URL <https://doi.org/10.1103/PhysRevB.73.060407>.
- 360 **37.** Radu, I., Stamm, C., Pontius, N., Kachel, T., Ramm, P., Thiele, J.-U., Dürr, H. A. & Back, C. H. Laser-
361 induced generation and quenching of magnetization on FeRh studied with time-resolved x-ray magnetic
362 circular dichroism. *Phys. Rev. B* **81**, 104415 (2010). URL <https://doi.org/10.1103/PhysRevB.81.104415>.
- 364 **38.** Mariager, S. O. *et al.* Structural and Magnetic Dynamics of a Laser Induced Phase Transition in FeRh. *Phys.*
365 *Rev. Lett.* **108**, 087201 (2012). URL <https://doi.org/10.1103/PhysRevLett.108.087201>.
- 366 **39.** Quirin, F., Vattilana, M., Shymanovich, U., El-Kamhawy, A. E., Tarasevitch, A., Hohlfeld, J., Von Der Linde, D.
367 & Sokolowski-Tinten, K. Structural dynamics in FeRh during a laser-induced metamagnetic phase transition.
368 *Phys. Rev. B* **85**, 020103(R) (2012). URL <https://doi.org/10.1103/PhysRevB.85.020103>.

- 369 **40.** Lee, J. S., Vescovo, E., Plucinski, L., Schneider, C. M. & Kao, C. C. Electronic structure and magnetic
370 properties of epitaxial FeRh(001) ultra-thin films on W(100). *Phys. Rev. B* **82**, 224410 (2010). URL <https://doi.org/10.1103/PhysRevB.82.224410>.
371
- 372 **41.** Gray, A. X. *et al.* Electronic structure changes across the metamagnetic transition in FeRh via hard X-ray
373 photoemission. *Phys. Rev. Lett.* **108**, 257208 (2012). URL [https://doi.org/10.1103/PhysRevLett.](https://doi.org/10.1103/PhysRevLett.108.257208)
374 [108.257208](https://doi.org/10.1103/PhysRevLett.108.257208).
- 375 **42.** Pressacco, F., Uhlíř, V., Gatti, M., Bendounan, A., Fullerton, E. E. & Sirotti, F. Stable room-temperature
376 ferromagnetic phase at the FeRh(100) surface. *Sci. Rep.* **6**, 22383 (2016). URL [https://doi.org/10.](https://doi.org/10.1038/srep22383)
377 [1038/srep22383](https://doi.org/10.1038/srep22383).
- 378 **43.** Maiti, K., Malagoli, M. C., Magnano, E., Dallmeyer, A. & Carbone, C. Electronic Band Structure of Gd:
379 A Consistent Description. *Phys. Rev. Lett.* **86**, 2846–2849 (2001). URL [https://doi.org/10.1103/](https://doi.org/10.1103/PhysRevLett.86.2846)
380 [PhysRevLett.86.2846](https://doi.org/10.1103/PhysRevLett.86.2846).
- 381 **44.** Beaulieu, N., Malinowski, G., Bendounan, A., Silly, M. G., Chauvet, C., Krizmancic, D. & Sirotti, F. Probing
382 ultrafast dynamics in electronic structure of epitaxial Gd(0001) on W(110). *J. Electron Spectrosc.* **189**, 40 – 45
383 (2013). URL <https://doi.org/10.1016/j.elspec.2013.06.005>.
- 384 **45.** Sirotti, F., Beaulieu, N., Bendounan, A., Silly, M. G., Chauvet, C., Malinowski, G., Fratesi, G., Vénier, V.
385 & Onida, G. Multiphoton *k*-resolved photoemission from gold surface states with 800-nm femtosecond laser
386 pulses. *Phys. Rev. B* **90**, 035401 (2014). URL <https://doi.org/10.1103/PhysRevB.90.035401>.
- 387 **46.** Pressacco, F., Uhlíř, V., Gatti, M., Nicolaou, A., Bendounan, A., Arregi, J. A., Patel, S. K. K., Fullerton, E. E.,
388 Krizmancic, D. & Sirotti, F. Laser induced phase transition in epitaxial FeRh layers studied by pump-probe
389 valence band photoemission. *Struct. Dyn.* **5**, 034501 (2018). URL [https://doi.org/10.1063/1.](https://doi.org/10.1063/1.5027809)
390 [5027809](https://doi.org/10.1063/1.5027809).
- 391 **47.** Sandratskii, L. M. & Mavropoulos, P. Magnetic excitations and femtomagnetism of FeRh: A first-principles
392 study. *Phys. Rev. B* **83**, 174408 (2011). URL <https://doi.org/10.1103/PhysRevB.83.174408>.
- 393 **48.** Gruner, M. E., Hoffmann, E. & Entel, P. Instability of the rhodium magnetic moment as the origin of the
394 metamagnetic phase transition in α – FeRh. *Phys. Rev. B* **67**, 064415 (2003). URL [https://doi.org/10.](https://doi.org/10.1103/PhysRevB.67.064415)
395 [1103/PhysRevB.67.064415](https://doi.org/10.1103/PhysRevB.67.064415).
- 396 **49.** Gu, R. Y. & Antropov, V. P. Dominance of the spin-wave contribution to the magnetic phase transition in FeRh.
397 *Phys. Rev. B* **72**, 012403 (2005). URL <https://doi.org/10.1103/PhysRevB.72.012403>.
- 398 **50.** Elliott, P., Müller, T., Dewhurst, J. K., Sharma, S. & Gross, E. K. U. Ultrafast laser induced local magneti-
399 zation dynamics in Heusler compounds. *Sci. Rep.* **6**, 38911 (2016). URL [https://doi.org/10.1038/](https://doi.org/10.1038/srep38911)
400 [srep38911](https://doi.org/10.1038/srep38911).
- 401 **51.** Dewhurst, J. K., Elliott, P., Shallcross, S., Gross, E. K. U. & Sharma, S. Laser-Induced Intersite Spin Transfer.
402 *Nano Lett.* **18**, 1842–1848 (2018). URL <https://doi.org/10.1021/acs.nanolett.7b05118>.
- 403 **52.** Hofherr, M. *et al.* Ultrafast optically induced spin transfer in ferromagnetic alloys. *Sci. Adv.* **6**, eaay8717 (2020).
404 URL <https://doi.org/10.1126/sciadv.aay8717>.
- 405 **53.** Uhlíř, V., Pressacco, F., Arregi, J. A., Procházka, P., Průša, S., Potoček, M., Šikola, T., Čechal, J., Bendounan,
406 A. & Sirotti, F. Single-layer graphene on epitaxial FeRh thin films. *Appl. Surf. Sci.* **514**, 145923 (2020). URL
407 <https://doi.org/10.1016/j.apsusc.2020.145923>.
- 408 **54.** Arregi, J. A., Caha, O. & Uhlíř, V. Evolution of strain across the magnetostructural phase transition in epitaxial
409 FeRh films on different substrates. *Phys. Rev. B* **101**, 174413 (2020). URL [https://doi.org/10.1103/](https://doi.org/10.1103/PhysRevB.101.174413)
410 [PhysRevB.101.174413](https://doi.org/10.1103/PhysRevB.101.174413).
- 411 **55.** Martins, M., Wellhöfer, M., Hoeft, J. T., Wurth, W., Feldhaus, J. & Follath, R. Monochromator beamline for
412 FLASH. *Rev. Sci. Instr.* **77**, 115108 (2006). URL <https://doi.org/10.1063/1.2364148>.

- 413 **56.** Gerasimova, N., Dziarzhyski, S. & Feldhaus, J. The monochromator beamline at FLASH: performance,
414 capabilities and upgrade plans. *J. Mod. Opt.* **58**, 1480–1485 (2011). URL [https://doi.org/10.1080/](https://doi.org/10.1080/09500340.2011.588344)
415 [09500340.2011.588344](https://doi.org/10.1080/09500340.2011.588344).
- 416 **57.** Ackermann, W. *et al.* Operation of a free-electron laser from the extreme ultraviolet to the water window. *Nat.*
417 *Photonics* **1**, 336–342 (2007). URL <https://doi.org/10.1038/nphoton.2007.76>.
- 418 **58.** Rossbach, J., Schneider, J. R. & Wurth, W. 10 years of pioneering X-ray science at the Free-Electron Laser
419 FLASH at DESY. *Phys. Rep.* **808**, 1 – 74 (2019). URL [https://doi.org/10.1016/j.physrep.](https://doi.org/10.1016/j.physrep.2019.02.002)
420 [2019.02.002](https://doi.org/10.1016/j.physrep.2019.02.002).
- 421 **59.** Kutnyakhov, D. *et al.* Time- and momentum-resolved photoemission studies using time-of-flight momentum
422 microscopy at a free-electron laser. *Rev. Sci. Instrum.* **91**, 013109 (2020). URL [https://doi.org/10.](https://doi.org/10.1063/1.5118777)
423 [1063/1.5118777](https://doi.org/10.1063/1.5118777).
- 424 **60.** Schönhense, G., Medjanik, K. & Elmers, H. J. Space-, time- and spin-resolved photoemission. *J. Electron*
425 *Spectros. Relat. Phenomena* **200**, 94–118 (2015). URL [https://doi.org/10.1016/j.elspec.2015.](https://doi.org/10.1016/j.elspec.2015.05.016)
426 [05.016](https://doi.org/10.1016/j.elspec.2015.05.016).
- 427 **61.** Giannozzi, P. *et al.* QUANTUM ESPRESSO: a modular and open-source software project for quantum
428 simulations of materials. *J. Phys.: Condens. Matter* **21**, 395502 (2009). URL [https://doi.org/10.](https://doi.org/10.1088/0953-8984/21/39/395502)
429 [1088/0953-8984/21/39/395502](https://doi.org/10.1088/0953-8984/21/39/395502).
- 430 **62.** Giannozzi, P. *et al.* Advanced capabilities for materials modelling with Quantum ESPRESSO. *J. Phys.: Condens.*
431 *Matter* **29**, 465901 (2017). URL <https://doi.org/10.1088/1361-648X/aa8f79>.
- 432 **63.** Marini, A., Hogan, C., Grüning, M. & Varsano, D. yambo: An ab initio tool for excited state calculations.
433 *Comput. Phys. Commun.* **180**, 1392–1403 (2009). URL [https://doi.org/10.1016/j.cpc.2009.](https://doi.org/10.1016/j.cpc.2009.02.003)
434 [02.003](https://doi.org/10.1016/j.cpc.2009.02.003).
- 435 **64.** Sangalli, D. & Marini, A. Ultra-fast carriers relaxation in bulk silicon following photo-excitation with a
436 short and polarized laser pulse. *Europhys. Lett.* **110**, 47004 (2015). URL [https://doi.org/10.1209/](https://doi.org/10.1209/0295-5075/110/47004)
437 [0295-5075/110/47004](https://doi.org/10.1209/0295-5075/110/47004).
- 438 **65.** Aschauer, U., Braddell, R., Brechbühl, S. A., Derlet, P. M. & Spaldin, N. A. Strain-induced structural instability
439 in FeRh. *Phys. Rev. B* **94**, 014109 (2016). URL <https://doi.org/10.1103/PhysRevB.94.014109>.
- 440 **66.** Wolloch, M. *et al.* Impact of lattice dynamics on the phase stability of metamagnetic FeRh: Bulk and thin films.
441 *Phys. Rev. B* **94**, 174435 (2016). URL <https://doi.org/10.1103/PhysRevB.94.174435>.
- 442 **67.** Zarkevich, N. A. & Johnson, D. D. FeRh ground state and martensitic transformation. *Phys. Rev. B* **97**, 014202
443 (2018). URL <https://doi.org/10.1103/PhysRevB.97.014202>.
- 444 **68.** Yeh, J. & Lindau, I. Atomic subshell photoionization cross sections and asymmetry parameters: $1 \leq Z \leq 103$.
445 *At. Data Nucl. Data Tables* **32**, 1 – 155 (1985). URL [https://doi.org/10.1016/0092-640X\(85\)](https://doi.org/10.1016/0092-640X(85)90016-6)
446 [90016-6](https://doi.org/10.1016/0092-640X(85)90016-6).
- 447 **69.** Sangalli, D. *et al.* Many-body perturbation theory calculations using the yambo code. *J. Phys.: Condens. Matter*
448 **31**, 325902 (2019). URL <https://doi.org/10.1088/1361-648x/2fab15d0>.

449 **Acknowledgements**

450 This work is dedicated to Wilfried Wurth, who passed away on May 8, 2019. We acknowledge support by the
451 scientific and technical staff of FLASH, as well as Holger Meyer and Sven Gieschen from University of Hamburg.
452 This work was supported by the excellence cluster “The Hamburg Centre for Ultrafast Imaging - Structure, Dynamics
453 and Control of Matter at the Atomic Scale” of the Deutsche Forschungsgemeinschaft (DFG EXC 1074) and through
454 the SFB 925 "Lichtinduzierte Dynamik und Kontrolle korrelierter Quantensysteme" (project B2). It received funding
455 from the EU-H2020 research and innovation program under European Union projects “MaX” Materials design at the
456 eXascale H2020-EINFRA-2015-1 (Grant Agreement No. 824143) and “NFFA” Nanoscience Foundries and Fine
457 Analysis-Europe H2020-INFRAIA-2014-2015 (Grant Agreement No. 654360) having benefited from the access
458 provided by the ISM node (CNR, Italy). We acknowledge the Deutsche Forschungsgemeinschaft (DFG, German
459 Research Foundation) – TRR 173 – 268565370 (projects A02 and A05). Access to the CEITEC Nano Research
460 Infrastructure was supported by the Ministry of Education, Youth and Sports (MEYS) of the Czech Republic
461 under the projects CEITEC 2020 (LQ1601) and CzechNanoLab (LM2018110). We acknowledge funding from the
462 Italian project MIUR PRIN Grant No. 20173B72NB. This work has received funding from the European Union’s
463 Horizon 2020 research and innovation program under the Marie Skłodowska-Curie and it is co-financed by the
464 South Moravian Region under grant agreement No. 665860.

465 **Author contributions**

466 F.P., V.U., J.A.A., M.G., D.S. and F.S. designed the project. F.P., D.K., M.H., S.Y.A., G.B., H.R., D.V., V.U., J.A.A.
467 and F.S. performed the time-resolved XPS experiments and analyzed the data. M.G., D.S. and A.M. designed the
468 theoretical approach to the problem. J.A.A. and V.U. prepared and characterized the samples. All authors discussed
469 the results. F.P., V.U., J.A.A., D.S., M.G. and F.S. wrote the paper with contributions from all authors and critical
470 revision from J.D., G.S. and W.W.

471 **Competing financial interests**

472 The authors declare no competing interests.

473 **Supplementary Information**

474 We provide four animations showing the simulated dynamics of charge density variations $n(\mathbf{r}, t) - n^{eq}(\mathbf{r})$ as
475 represented in panels **a** and **b** of Fig.5 during two time-windows. The first time window ($-65 \text{ fs} < t < -55 \text{ fs}$)
476 corresponds to the beginning of the photoexcitation process and shows the laser-induced charge oscillations
477 for about four periods of the main laser frequency (for $\lambda = 800 \text{ nm}$, $T = 2.67 \text{ fs}$). During this time window,
478 $n(\mathbf{r}, t) - n^{eq}(\mathbf{r}) \sim 10^{-7}$ a.u. (see **Supplementary Videos 1 & 2**). The second time window ($135 \text{ fs} < t < 137.5 \text{ fs}$) is
479 close to the end of the optical pulse where a persistent change of the charge density is observed. This variation is due
480 to the update of the mean field felt by the electrons, which redistribute accordingly in the unit cell. Laser-induced
481 charge oscillations are still present, but only constitute a correction on top of the much larger persistent variation. At
482 the end of the laser pulse, $n(\mathbf{r}, t) - n^{eq}(\mathbf{r}) \sim 10^{-5}$ a.u. (see **Supplementary Videos 3 & 4**.)

Figures

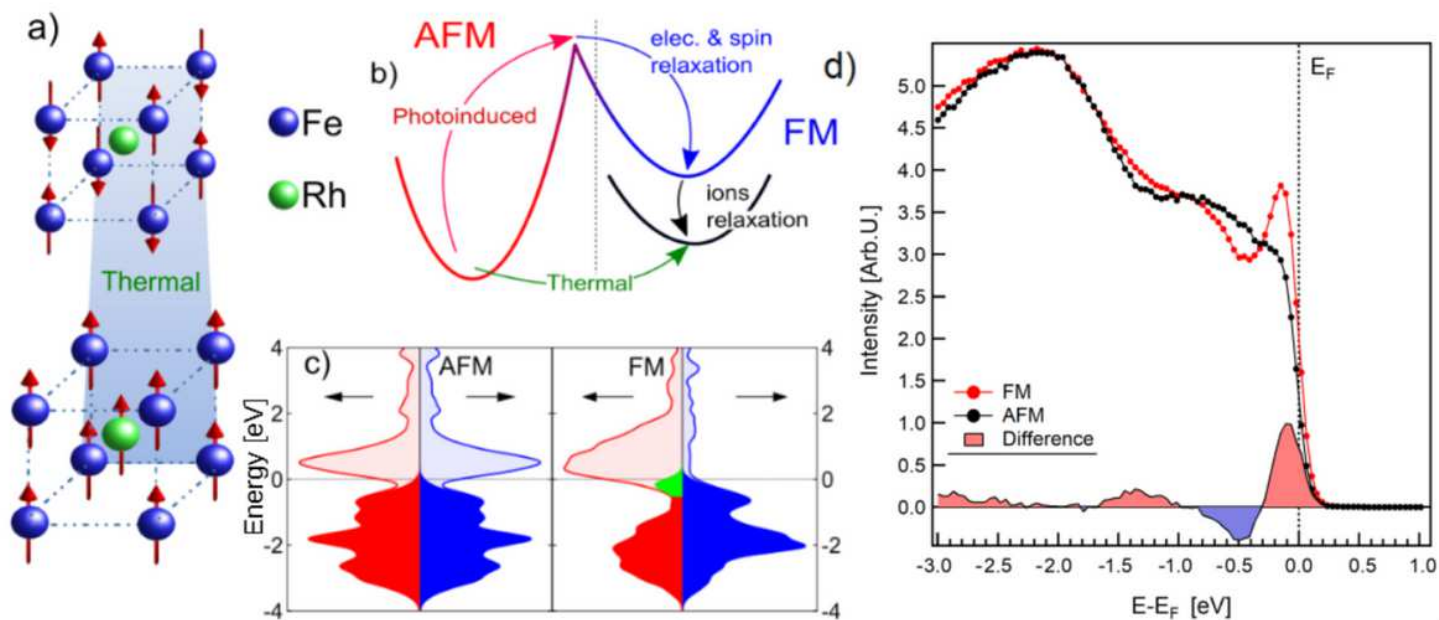


Figure 1

Electronic properties of FeRh across the metamagnetic phase transition. (a) Sketch of the isostructural metamagnetic phase transition in FeRh. At room temperature (top) the system is AFM showing atomic magnetic moments only at the Fe atom sites ($m_{\text{Fe}} = \pm 3.3 \mu\text{B}$). Above 360 K (bottom) the system has ferromagnetically coupled magnetic moments at the Fe ($m_{\text{Fe}} = 3.1 \mu\text{B}$) and Rh ($m_{\text{Rh}} = 0.9 \mu\text{B}$) sites. The whole unit cell expands isotropically by about 1% in volume²⁷. (b) Schematic representation of the two possible paths in the AFM to FM phase transition: direct thermally-driven transition to the FM phase (green arrow), and two-step transition going through a transient electronic state reached during photoexcitation (red arrow) followed by relaxation to the equilibrium FM state (blue and black arrows). (c) Calculated spin-resolved electronic density of states in the AFM and FM phases. The filled areas represent the electronic occupation at thermal equilibrium, with the green area highlighting the position of the Fe minority band (see manuscript text). (d) Measured x-ray photoelectron spectra of FeRh in the AFM (black dots) and FM (red dots) phase. The solid curve at the bottom of the graph is the difference between the two spectra, which allows to appreciate the relative electron density change across the transition. The data correspond to quasi-static thermal cycling experiments prior to the time-resolved measurements.

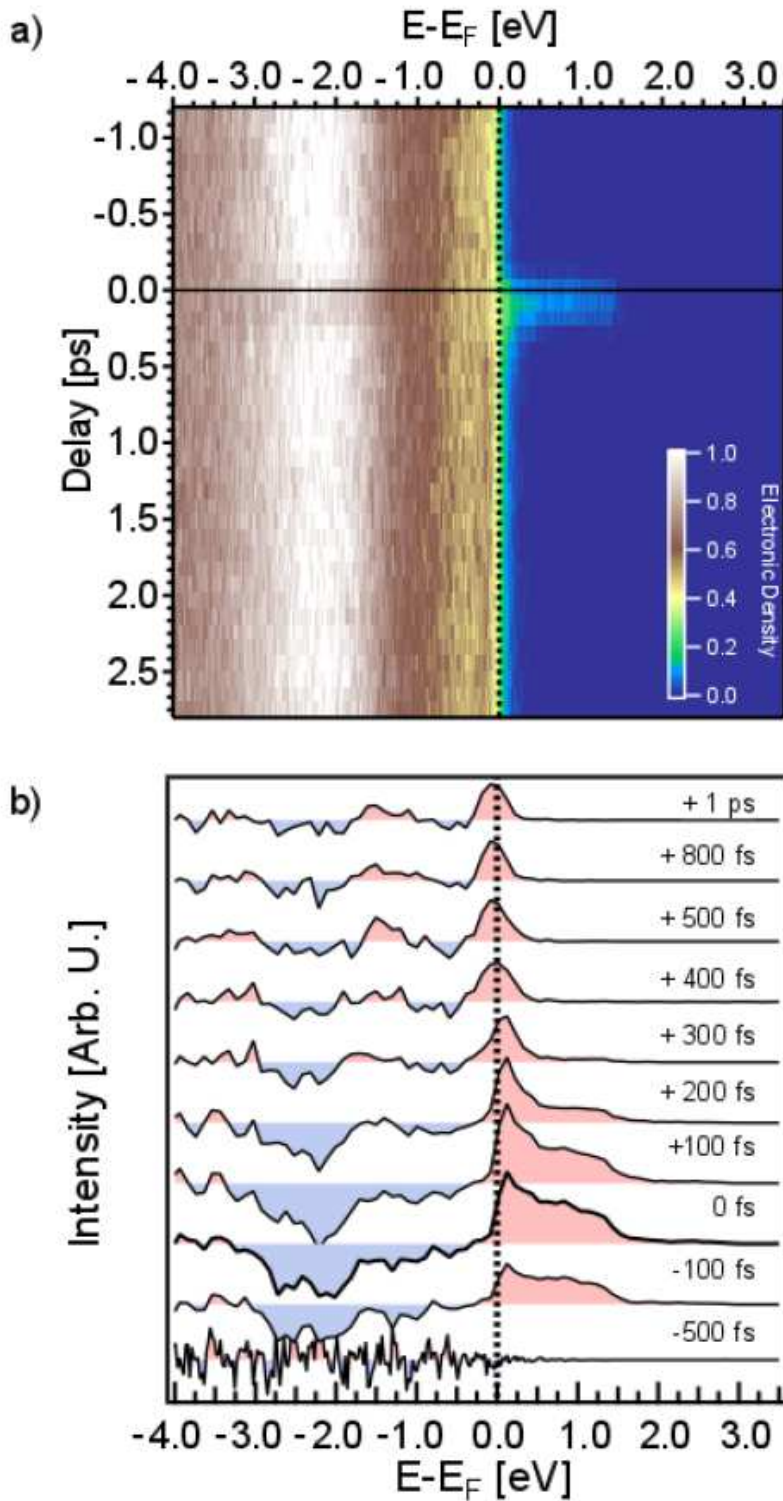


Figure 2

Time-resolved x-ray photoelectron spectroscopy at room temperature. (a) Energy- and delay-dependent matrix of the measured spectra. The vertical dashed line marks the position of the Fermi level E_F , while the horizontal solid line designates the time zero, t_0 . The appearance of electronic density in the unoccupied states is a fingerprint of the laser excitation. We used this spectral feature to identify the temporal overlap between the optical pump and the x-ray probe pulses. (b) Differential photoelectron

spectra at selected delays. To enhance the signal to noise ratio, we average the unpumped spectra (between -1 ps and -0.5 ps) and subtract the average spectrum from each row of the matrix. This allows evaluating the statistical noise at negative time delays (-500 fs) as well as accentuating the temporal evolution of the photoelectron spectra. Red and blue shaded areas indicate an increase and a reduction of the electron density with respect to the spectra at negative delays, respectively.

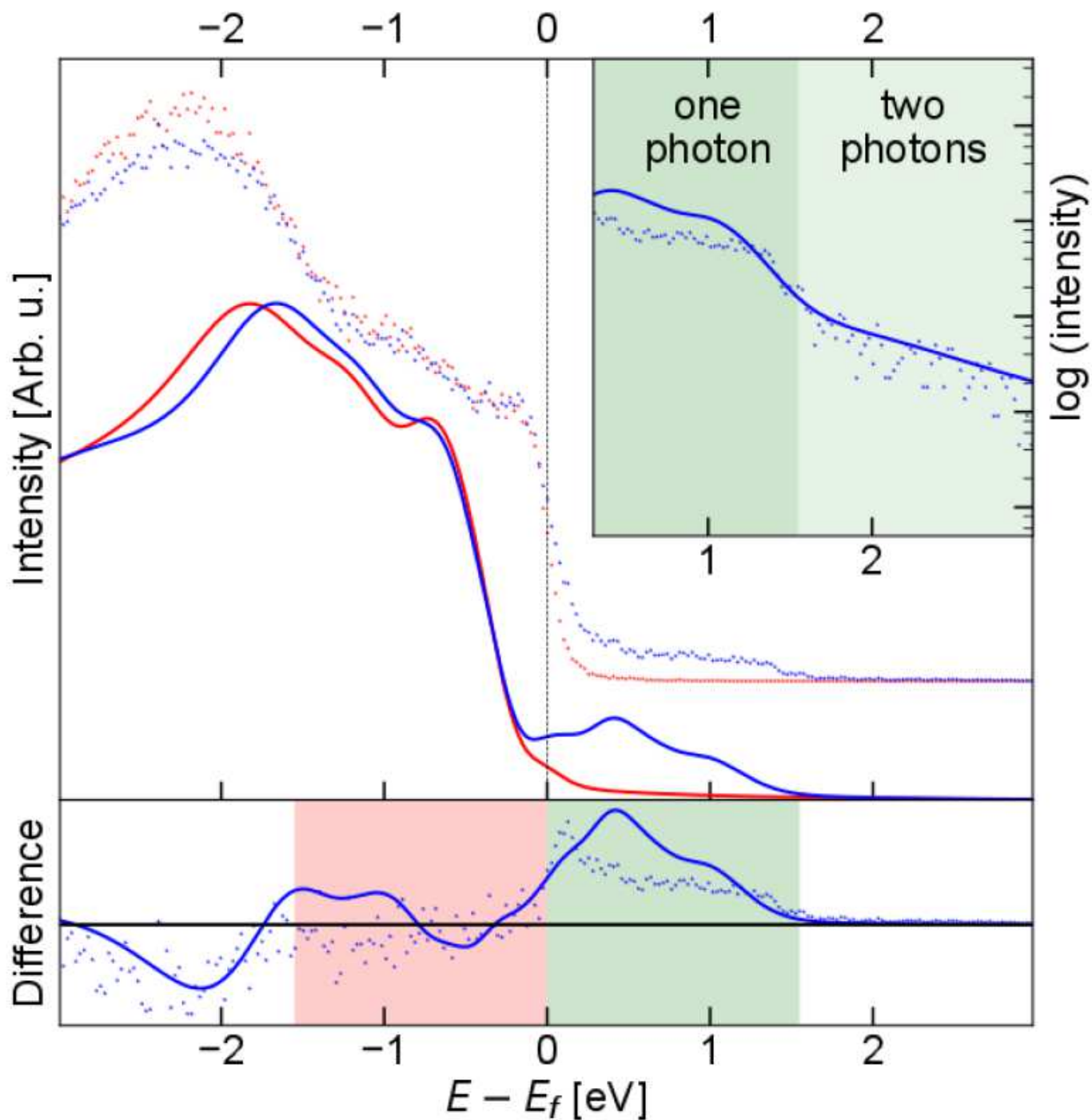


Figure 3

Comparison of experimental and computed photoelectron spectra of FeRh. Spectra at equilibrium ($t = -0.5$ ps) and at the maximum of the pump pulse ($t = 0$ ps) are shown in linear (top panel) and logarithmic scales (inset). The bottom panel exhibits the difference between the two spectra in the top panel. The green (red) region represents the energy range to (from) which electrons are excited with one-photon (1.55 eV) processes. The light green region in the top panel inset identifies the energy range that can be reached by two-photon (3.1 eV) processes.

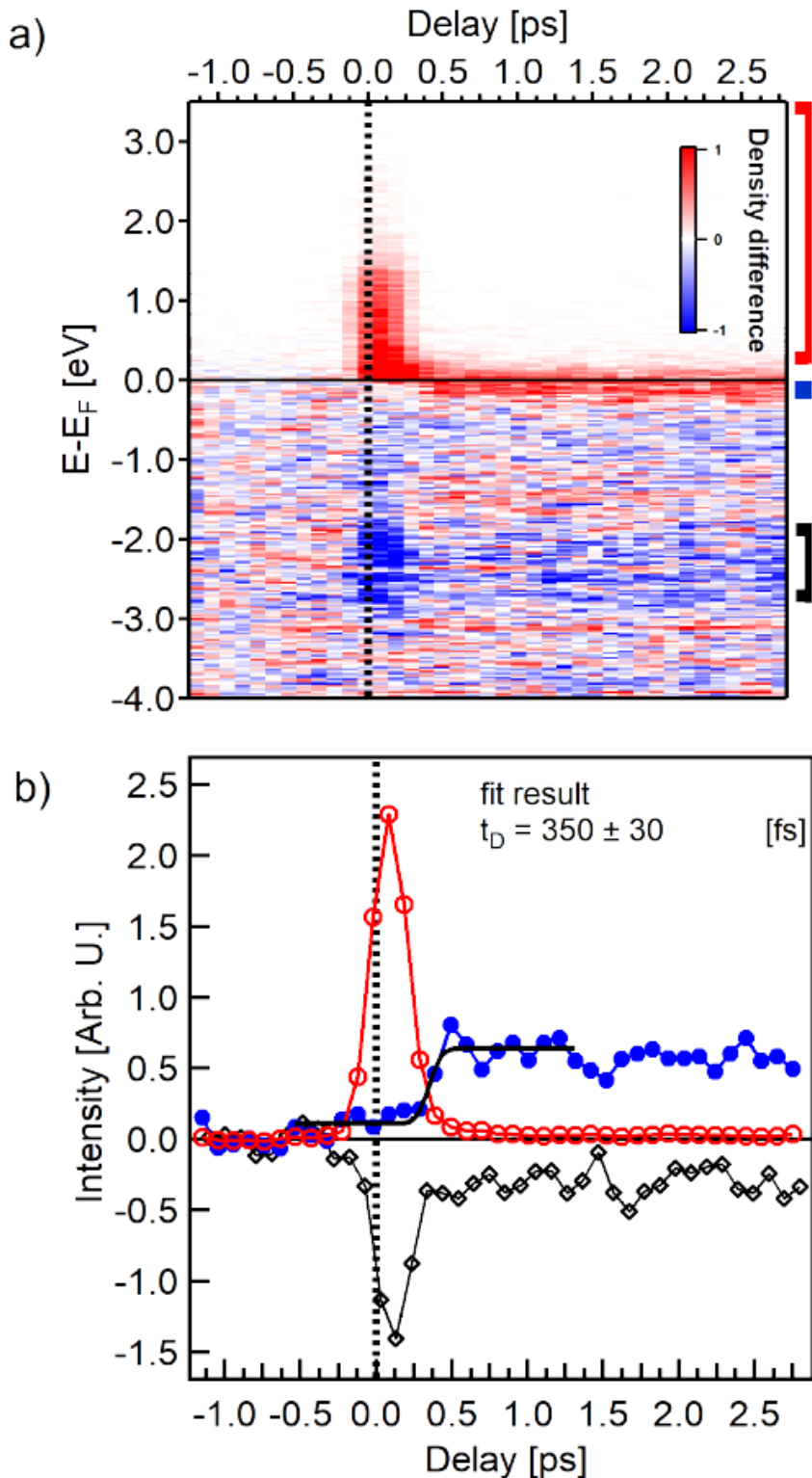


Figure 4

Subpicosecond generation of the electronic FM order in FeRh. (a) Energy- and delay-dependent differential matrix of the measured photoelectron spectra. We subtracted the average of unpumped spectra (between -1 ps and -0.5 ps) from each measured spectrum. The effect of laser excitation is evident around time zero, indicating depletion of the occupied states and the corresponding population of the empty states. In addition, an increase in the electronic density close to the Fermi level is observed at positive time delays. The red, blue, and black bars on the right hand side mark the representative integration regions for tracking the electronic dynamics in the unoccupied states, the formation of the Fe minority peak, and the modification of the deeper bands, respectively. (b) Temporal evolution of the electronic density in the three characteristic energy regions marked in (a). The population of states above the Fermi level shows a fast rise and a consecutive decay around t_0 (empty red circles). The deeper bands (empty black diamonds) show a corresponding depletion and recovery which reflects the dynamics of the unoccupied states. However, their occupation level stabilizes 300 fs after t_0 and remains constant thereafter. The electronic density slightly below E_F (filled blue circles) shows a moderate increase during the laser excitation up to 300 fs delay, followed by a pronounced increase due to the shift of Fe minority band below E_F at a delay t_D of 350 fs. This value was extracted by fitting the error function to the experimental results (black solid line). Subsequently, the minority Fe band peak intensity remains constant throughout the investigated delay range.

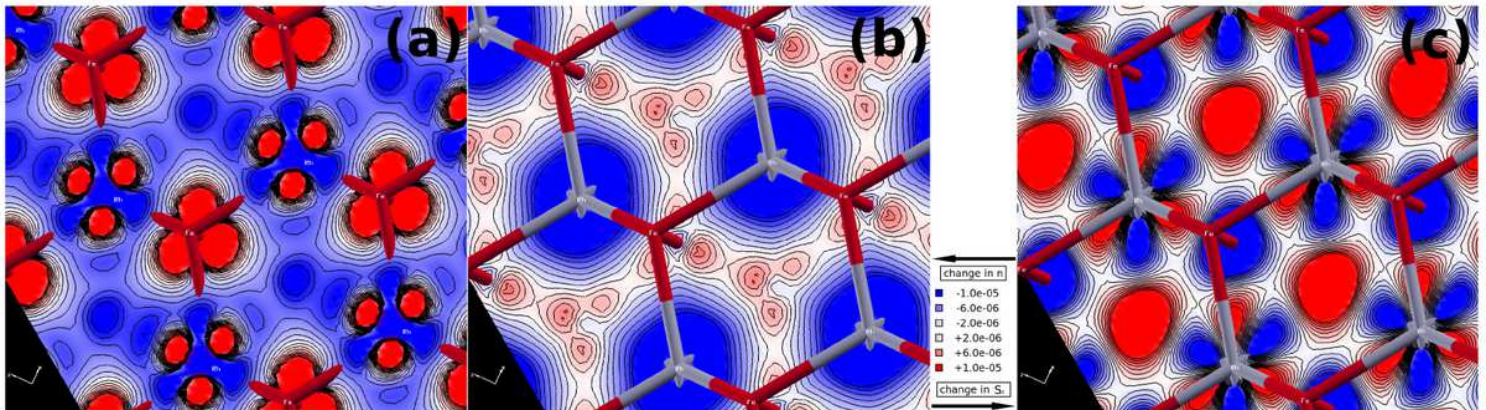


Figure 5

Computed photoinduced changes in charge and spin density in FeRh. (a, b) Changes in the charge density $n(r,tf) - n_{eq}(r)$ and (c) spin density $S_z(r,tf) - S_{zeq}(r)$ at the end of the laser pulse ($t = t_f$) with respect to the equilibrium configuration. Densities are represented in atomic units on two different FeRh{111}-planes: the plane just below the Fe atoms (panel a) and the plane containing the Rh atoms (panels b, c). Fe and Rh atom positions are indicated by red and grey segments of the lattice, respectively. Charge is transferred from the occupied (bonding) orbitals of Rh atoms (panel b), to the unoccupied (anti-bonding) orbitals of Rh and Fe (panel a). Since the Fe anti-bonding levels are filled in this process, the local Fe spin density is reduced. As a result, there is a redistribution of spin density around the Rh atoms and a reduction of the local spin moment at the Fe atoms (panel c). The movies in the Supplementary Information show the simulated time evolution of the charge density variations at the Fe and Rh sites as represented in panels (a) and (b) at the beginning and the end of the laser pulse.

Supplementary Files

This is a list of supplementary files associated with this preprint. Click to download.

- [Video1.avi](#)
- [Video3.avi](#)